Inorganic Chemistry

ARTICLE

pubs.acs.org/IC

Pentavalent and Tetravalent Uranium Selenides, $Tl_3Cu_4USe_6$ and $Tl_2Ag_2USe_4$: Syntheses, Characterization, and Structural Comparison to Other Layered Actinide Chalcogenide Compounds

Daniel E. Bugaris,[†] Eun Sang Choi,[‡] Roy Copping,[§] Per-Anders Glans,[||] Stefan G. Minasian,[§,⊥] Tolek Tyliszczak,[||] Stosh A. Kozimor,[⊥] David K. Shuh,[§] and James A. Ibers*[,†]

[†]Department of Chemistry, Northwestern University, 2145 Sheridan Road, Evanston, Illinois 60208-3113, United States

[‡]Department of Physics and National High Magnetic Field Laboratory, Florida State University, Tallahassee, Florida 32310, United States

[§]Chemical Sciences Division, Lawrence Berkeley National Laboratory, Berkeley, California 94720, United States

[||]Advanced Light Source, Lawrence Berkeley National Laboratory, Berkeley, California 94720, United States

[⊥]Chemistry Division, Los Alamos National Laboratory, Los Alamos, New Mexico 87545, United States

S *Supporting Information*

ABSTRACT: The compounds $Tl_3Cu_4USe_6$ and $Tl_2Ag_2USe_4$ were synthesized by the reaction of the elements in excess TlCl at 1123 K. Both compounds crystallize in new structure types, in space groups $P2_1/c$ and $C2/m$, respectively, of the monoclinic system. Each compound contains layers of USe_6 octahedra and MSe_4 (M = Cu, Ag) tetrahedra, separated by Tl^+ cations. The packing of the octahedra and the tetrahedra within the layers is compared to the packing arrangements found in other layered actinide chalcogenides. $Tl_3Cu_4USe_6$ displays peaks in its magnetic susceptibility at 5 and 70 K. It exhibits modified Curie–Weiss paramagnetic behavior with an effective moment of 1.58(1) μ_B in the temperature range 72–300 K, whereas $Tl_2Ag_2USe_4$ exhibits modified Curie–Weiss paramagnetic behavior with μ_{eff} = 3.4(1) μ_B in the temperature range 100–300 K. X-ray absorption near-edge structure (XANES) results from scanning transmission X-ray spectromicroscopy confirm that $Tl_3Cu_4USe_6$ has Se bonding characteristic of discrete Se^{2-} units, Cu bonding generally representative of Cu^+, and U bonding consistent with a U^{4+} or U^{5+} species. On the basis of these measurements, as well as bonding arguments, the formal oxidation states for U may be assigned as +5 in $Tl_3Cu_4USe_6$ and +4 in $Tl_2Ag_2USe_4$

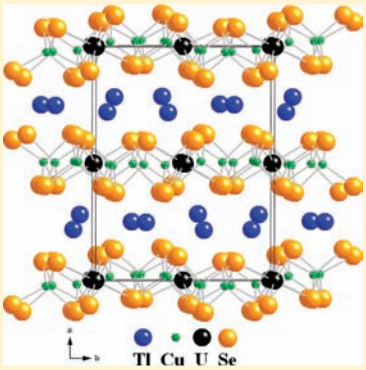

INTRODUCTION

The vast majority of quaternary uranium chalcogenides (Q = chalcogen = S, Se, Te) also incorporate a transition metal and an alkali metal or an alkaline-earth metal.[1] Theoretical calculations for the $AMUQ_3$ (A = K, Rb, Cs; M = Cu, Ag; Q = S, Se) compounds show that the electrons from A make little contribution to the density of states (DOS) near the Fermi level.[2] Furthermore, it is to be expected that an s-block element will have a negligible effect on the magnetic behavior of a compound. In the search for new quaternary uranium chalcogenides, it is desirable to replace the alkali metal or alkaline-earth metal with a p-block element, or ultimately, a second transition metal or a lanthanide.

The most obvious candidate for achieving this goal is to replace the alkali metal with thallium. Tl prefers the +1 oxidation state similar to the alkali metals and exhibits other chemical similarities as well.[3] However, there are two significant differences between Tl and the alkali metals. First, because the electronegativity of Tl is much larger than that of the alkali metals (2.04 vs 0.98 for Li),[4] the bonding in the resultant compound should be more covalent. Second, Tl^+ possesses a lone pair of electrons that can display stereoactivity, a feature lacking for the alkali metals. Both of these differences may contribute to more complex structures in the quaternary uranium chalcogenide system. There is precedent for such ternary phases, such as TlU_2Se_6[5] and $Tl_{0.56}UTe_3$.[6]

We report here the syntheses, structures, and characterization of the new compounds $Tl_3Cu_4USe_6$ and $Tl_2Ag_2USe_4$ as well as provide a comparison to known layered quaternary actinide chalcogenides. We present evidence that the formal oxidation state of U is +5 in $Tl_3Cu_4USe_6$ and +4 in $Tl_2Ag_2USe_4$.

EXPERIMENTAL METHODS

Syntheses. ***Caution!*** *Great care must be exercised when handling Tl and its compounds. When exposed to moisture, Tl forms TlOH, which is soluble in water and is easily absorbed through the skin. Thus, contact with*

Received: March 18, 2011
Published: June 16, 2011

skin is to be carefully avoided, and appropriate gloves (e.g., nitrile) should always be worn when handling Tl compounds.

Finely divided uranium powder was prepared by a modification of the literature procedure.[7] Uranium metal turnings (depleted, Oak Ridge National Laboratory) were washed with concentrated HNO_3 to remove any coating of uranium oxide. The turnings were then rinsed with deionized water and dried with acetone. The turnings were placed in a Schlenk vessel and reacted with an atmosphere of H_2 at 723 K to produce UH_3. UH_3 was converted to finely divided U powder under vacuum conditions at 773 K.

The remaining reactants were used as-obtained from the manufacturers. Reactions were performed in carbon-coated fused-silica tubes. The tubes were charged with reaction mixtures under an Ar atmosphere in a glovebox. The tubes were evacuated to 10^{-4} Torr and flame-sealed, before being placed in a computer-controlled furnace. Selected single crystals from each reaction were examined by means of energy dispersive X-ray (EDX) analyses on a Hitachi S-3400 SEM.

Synthesis of $Tl_3Cu_4USe_6$. The reaction mixture consisted of U (0.13 mmol), Cu (0.25 mmol; Aldrich, 99.5%), Se (0.5 mmol; Cerac, 99.999%), and TlCl (0.83 mmol; Strem Chemicals). The reaction mixture was placed in the furnace where it was heated to 1123 K over 26 h, kept at 1123 K for 7 days, and cooled at 2 K h^{-1} to 473 K, and then the furnace was turned off. The product consisted of golden black blocks of $Tl_3Cu_4USe_6$ in about 10 wt % yield (based on Cu). Additionally, green UCl_4 was formed, which decomposed in moist air. EDX analysis of selected crystals showed the presence of Tl, Cu, U, and Se but not of Cl. The compound is moderately stable in air.

Synthesis of $Tl_2Ag_2USe_4$. The reaction mixture consisted of U (0.13 mmol), Ag (0.25 mmol; Aldrich, 99.99+%), Se (0.5 mmol), and TlCl (0.83 mmol). The reaction mixture was placed in the furnace where it was subjected to the same heating profile as above. The product consisted of long black needles of $Tl_2Ag_2USe_4$ in about 20 wt % yield (based on U). EDX analysis of selected crystals showed the presence of Tl, Ag, U, and Se but not of Cl. The compound is moderately stable in air.

Structure Determinations. Single-crystal X-ray diffraction data were collected with the use of graphite-monochromatized Mo Kα radiation (λ = 0.71073 Å) at 100 K on a Bruker APEX2 CCD diffractometer.[8] The crystal-to-detector distance was 5.023 cm. Crystal decay was monitored by recollecting the 50 initial frames at the end of the data collection. Data were collected by a scan of 0.3° in ω in groups of 606 frames at φ settings of 0°, 90°, 180°, and 270°. The exposure time was 20 s/frame for both compounds. The collection of intensity data was carried out with the use of the program APEX2.[8] Cell refinement and data reduction were carried out with the use of the program SAINT v7.23a in APEX2.[8] Face-indexed absorption corrections were performed numerically with the use of the program SADABS.[9] Then, the program SADABS[9] was employed to make incident beam and decay corrections. The structures were solved with the direct methods program SHELXS and refined with the least-squares program SHELXL.[10] Each final refinement included anisotropic displacement parameters and a secondary extinction correction. The program STRUCTURE TIDY[11] was used to standardize the positional parameters. Additional experimental details are given in Table 1 and the Supporting Information. Selected metrical details are presented in Tables 2 and 3.

Magnetic Susceptibility Measurement. Magnetic susceptibility as a function of temperature was measured on samples of ground single crystals of $Tl_3Cu_4USe_6$ (5.00 mg) and $Tl_2Ag_2USe_4$ (5.71 mg) with the use of a Quantum Design MPMS XL-7 SQUID magnetometer. The samples were loaded into gelatin capsules. For $Tl_3Cu_4USe_6$, field-cooled (FC) susceptibility data were collected between 2 and 300 K at applied fields of 500 G, 1 kG, 10 kG, 20 kG, 40 kG, and 70 kG. Zero field-cooled (ZFC) susceptibility data were collected only at an applied field of 1 kG. For $Tl_2Ag_2USe_4$, both ZFC and FC susceptibility data were collected between 2 and 300 K at an applied field of 500 G.

Table 1. Crystal Data and Structure Refinements for $Tl_3Cu_4USe_6$ and $Tl_2Ag_2USe_4$[a]

	$Tl_3Cu_4USe_6$	$Tl_2Ag_2USe_4$
fw	1579.06	1178.35
space group	$P2_1/c$	$C2/m$
Z	4	2
a (Å)	14.962(3)	14.4919(5)
b (Å)	11.400(2)	4.2301(2)
c (Å)	7.6223(2)	9.4745(4)
β (deg)	94.32(3)	127.300(1)
V (Å^3)	1296.5(4)	462.02(3)
ρ_c (g cm^{-3})	8.090	8.470
μ (mm^{-1})	72.808	72.058
$R(F)$[b]	0.0449	0.0371
$R_w(F_o^2)$[c]	0.0996	0.1196

[a] For both structures, T = 100(2) K and λ = 0.71073 Å. [b] $R(F) = \Sigma||F_o| - |F_c||/\Sigma|F_o|$ for $F_o^2 > 2\sigma(F_o^2)$. [c] For $F_o^2 < 0$, $w^{-1} = \sigma^2(F_o^2)$; for $F_o^2 \geq 0$, $w^{-1} = \sigma^2(F_o^2) + (0.03 \times F_o^2)^2$ ($Tl_3Cu_4USe_6$) and $w^{-1} = \sigma^2(F_o^2) + (0.04 \times F_o^2)^2$ ($Tl_2Ag_2USe_4$).

Table 2. Selected Interatomic Distances (Å) and Angles (deg) for $Tl_3Cu_4USe_6$

Cu(1)−Se(1)	2.434(2)	U(1)−Se(1) × 2	2.725(2)
Cu(1)−Se(2)	2.582(3)	U(1)−Se(2) × 2	2.806(1)
Cu(1)−Se(3)	2.427(2)	U(1)−Se(3) × 2	2.832(2)
Cu(1)−Se(3)	2.557(2)	U(2)−Se(4) × 2	2.726(2)
Cu(2)−Se(1)	2.516(2)	U(2)−Se(5) × 2	2.771(1)
Cu(2)−Se(2)	2.457(2)	U(2)−Se(6) × 2	2.850(2)
Cu(2)−Se(2)	2.481(2)		
Cu(2)−Se(3)	2.440(2)	Tl···Se	2.990(2)−3.670(2)
Cu(3)−Se(4)	2.439(2)	Cu(1)···Cu(1)	2.597(4)
Cu(3)−Se(5)	2.604(2)	Cu(1)···Cu(2)	2.582(3)
Cu(3)−Se(6)	2.447(2)	Cu(1)···Cu(2)	2.618(3)
Cu(3)−Se(6)	2.563(2)	Cu(3)···Cu(3)	2.571(3)
Cu(4)−Se(4)	2.511(2)	Cu(3)···Cu(4)	2.627(3)
Cu(4)−Se(5)	2.477(2)	Cu(3)···Cu(4)	2.654(3)
Cu(4)−Se(5)	2.498(2)		
Cu(4)−Se(6)	2.440(2)	Se−Cu−Se	98.66(8)−124.68(8)

Table 3. Selected Interatomic Distances (Å) and Angles (deg) for $Tl_2Ag_2USe_4$

Ag−Se(1) × 2	2.671(2)	Se(1)−Ag−Se(1)	104.73(8)
Ag−Se(1)	2.799(2)	Se(1)−Ag−Se(1)	115.91(5)
Ag−Se(2)	2.638(2)	Se(1)−Ag−Se(2)	104.93(6)
U−Se(1) × 2	2.853(2)	Se(1)−Ag−Se(2)	109.36(7)
U−Se(2) × 4	2.881(1)	Se(1)−U−Se(1)	180
		Se(1)−U−Se(2)	85.52(4)
Ag···Ag	2.904(2)	Se(2)−U−Se(2)	85.53(5)
Tl···Se	3.120(2)−3.618(2)	Se(2)−U−Se(2)	180

Scanning Transmission X-ray Microscopy (STXM) Spectromicroscopy. STXM spectromicroscopy at the Advanced Light Source-Molecular Environmental Sciences (ALS-MES) Beamline 11.0.2 was utilized to record images, elemental maps, and X-ray absorption near-edge structure (XANES) spectra at the Se $2p_{3/2,1/2}$ edges ($L_{3,2}$), Cu 2p$_{3/2,1/2}$ edges (L$_{3,2}$), and U 4d$_{5/2,3/2}$ edges (N$_{5,4}$) from $\mathrm{Tl_3Cu_4USe_6}$ to obtain element-specific oxidation state information.[12−15] No XANES spectra were obtainable from soft X-ray core levels of the Tl N$_{1-7}$ (4s, 4p, 4d, and 4f edges, respectively). The radioactive samples were powdered and sealed between two thin (100 nm) silicon nitride windows with epoxy before transfer to the He-purged STXM instrument. The spatial resolution for the Cu and U images and spectra was ~40 nm, whereas for Se spectromicroscopy, it was ~50 nm. The errors in peak energy assignments are 0.05 eV for Cu and U spectra and 0.13 eV for the Se spectra (refer to the Supporting Information for additional experimental details). The ALS-MES STXM data collection has been described in detail; spectra were extracted from image stacks (a complete set of registered images collected sequentially at each photon energy of a spectral scan).[16] No sample degradation was observed during the period of data collection. All spectra were normalized to the incoming flux by integrating over areas without sample particulates. XANES spectra had linear backgrounds subtracted; they were then smoothed and renormalized as described below. The ALS operated at 500 mA of continuously stored electron beam during data collection. The following U reference materials for XANES spectra were synthesized according to literature procedures: β-$\mathrm{USe_2}$,[17] $\mathrm{USe_3}$,[18] and $\mathrm{RbAuUSe_3}$.[19] $\mathrm{(UO_2)_4O(OH)_6 \cdot 6H_2O}$ (Schoepite) was obtained from material prepared at LBNL. The Cu reference materials, $\mathrm{Cu_2O}$ and CuSe, were obtained from Alfa Aesar, whereas CuO was obtained from Baker.

■ RESULTS AND DISCUSSION

Syntheses. Golden black single crystals of $\mathrm{Tl_3Cu_4USe_6}$ were obtained in 10 wt % yield by the reaction of U, Cu, Se, and excess TlCl at 1123 K. The reaction carried out under identical conditions, but with Ag substituted for Cu, produced long black needles of $\mathrm{Tl_2Ag_2USe_4}$ in approximately 20 wt % yield. Efforts to synthesize the sulfide and telluride analogues of either compound were unsuccessful.

There are numerous examples in the literature of the use of alkali halide or alkaline-earth halide salts as fluxes in solid-state syntheses of chalcogenides. Often, the halide salt is added to the reaction mixture to aid in the crystallization of the targeted product. For example, the syntheses of $\mathrm{U_3Te_5}$,[20] $\mathrm{Cu_{0.78}U_2Te_6}$,[21] $\mathrm{Ba_2Cu_2US_5}$,[22] and $\mathrm{BaCuDyTe_3}$[23] require the uses of CsCl, KI, NaBr, and $\mathrm{BaCl_2}$, respectively. Less commonly, the halide salt is added in excess not only to aid in crystallization but also as a source of either an alkali-metal element or an alkaline-earth element. $\mathrm{KCuUS_3}$[2] and $\mathrm{CsAuUTe_3}$[19] were synthesized with an excess of KBr and CsCl, respectively, as opposed to the much more common route involving alkali-metal polychalcogenides,[24] which was used for all other U-containing compounds of the $\mathrm{KCuZrS_3}$ structure type.[25]

The current compounds, $\mathrm{Tl_3Cu_4USe_6}$ and $\mathrm{Tl_2Ag_2USe_4}$, are the first solid-state thallium chalcogenides to be synthesized with the use of excess TlCl as a reactive flux. Previous syntheses of thallium chalcogenides had involved either Tl metal[26] or binary Tl chalcogenides.[6,27] How the reaction of U, Cu or Ag, and Se with TlCl proceeds is not known. It is clear that some Tl is incorporated into the final quaternary products, and that $\mathrm{UCl_4}$ is formed. The $\mathrm{UCl_4}$ decomposes upon exposure to moist air, and the major products, $\mathrm{Tl_3Cu_4USe_6}$ and $\mathrm{Tl_2Ag_2USe_4}$, can be mechanically separated from the reaction mixtures.

Structure of $\mathrm{Tl_3Cu_4USe_6}$. $\mathrm{Tl_3Cu_4USe_6}$ crystallizes in a new structure type (Figure 1) in space group $P2_1/c$ of the monoclinic system. The asymmetric unit comprises two U atoms, each at an inversion center, along with three Tl, four Cu, and six Se atoms, all in general positions. Each U atom is octahedrally coordinated by six Se atoms. Each Cu atom is tetrahedrally coordinated by four Se atoms. Atoms Tl(1) and Tl(2) are coordinated to six Se atoms in a trigonal prism, and atom Tl(3) is coordinated to seven Se atoms with a capped trigonal prismatic geometry. The structure consists of ${}^{2}_{\infty}[\mathrm{Cu_4USe_6}^{3-}]$ layers separated by $\mathrm{Tl^+}$ cations. There are alternating layers of U(1)$\mathrm{Se_6}$ octahedra with Cu(1)$\mathrm{Se_4}$ and Cu(2)$\mathrm{Se_4}$ tetrahedra and U(2)$\mathrm{Se_6}$ octahedra with Cu(3)$\mathrm{Se_4}$ and Cu(4)$\mathrm{Se_4}$ tetrahedra. Within the ${}^{2}_{\infty}[\mathrm{Cu_4USe_6}^{3-}]$ layer (Figure 2), each $\mathrm{USe_6}$ octahedron shares six edges and four corners with the surrounding $\mathrm{CuSe_4}$ tetrahedra. The Cu(1,3)$\mathrm{Se_4}$ tetrahedra share one edge and two corners with $\mathrm{USe_6}$ octahedra, as well as three edges and one corner with $\mathrm{CuSe_4}$ tetrahedra. The Cu(2,4)$\mathrm{Se_4}$ tetrahedra share two edges with $\mathrm{USe_6}$ octahedra, as well as two edges and three corners with $\mathrm{CuSe_4}$ tetrahedra. Within the ${}^{2}_{\infty}[\mathrm{Tl_3Se_6}^{9-}]$ layer, each Tl(1)$\mathrm{Se_6}$ trigonal prism shares two faces, two edges, and three corners with neighboring polyhedra. Each Tl(2)$\mathrm{Se_6}$ trigonal prism shares one face, five edges, and one corner with adjacent polyhedra, and the Tl(3)$\mathrm{Se_7}$ capped trigonal prism shares one face, five edges, and two corners with its neighbors. There are no Se−Se bonds in the structure. The shortest Se···Se interaction is 4.15 Å.

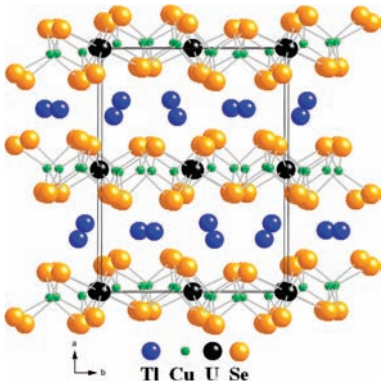

Figure 1. The crystal structure of $\mathrm{Tl_3Cu_4USe_6}$, viewed down c^*.

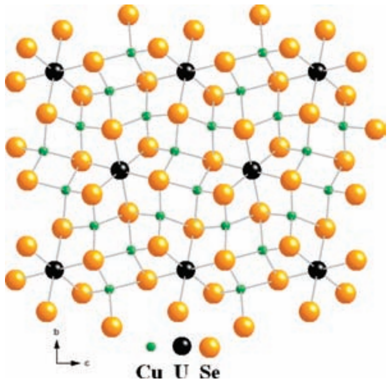

Figure 2. The two-dimensional ${}^{2}_{\infty}[\mathrm{Cu_4USe_6}^{3-}]$ layer in $\mathrm{Tl_3Cu_4USe_6}$, viewed down a^*.

Structure of $\mathrm{Tl_2Ag_2USe_4}$. $\mathrm{Tl_2Ag_2USe_4}$ crystallizes in space group $C2/m$ of the monoclinic system in a new structure type. The structure of this compound (Figure 3) is closely related to the $\mathrm{K_2Cu_2CeS_4}$ structure type,[28] which is also in the space group $C2/m$. The two structures display the same layers (${}^{2}_{\infty}[\mathrm{Ag_2USe_4}^{6-}]$ and ${}^{2}_{\infty}[\mathrm{Cu_2CeS_4}^{6-}]$), but these are packed differently. $\mathrm{Tl_2Ag_2USe_4}$ possesses cell constants that are similar to those of $\mathrm{TaTe_2}$;[29]

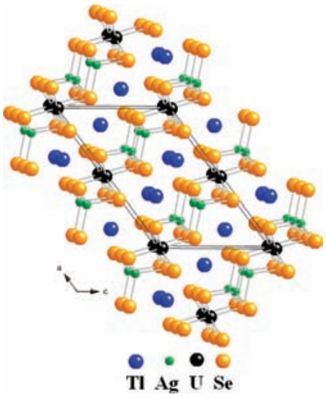

Figure 3. The crystal structure of $Tl_2Ag_2USe_4$, viewed down *b*.

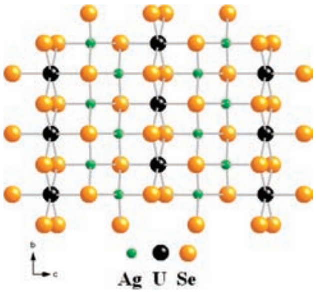

Figure 4. The two-dimensional ${}^{2}_{\infty}[Ag_2USe_4{}^{2-}]$ layer in $Tl_2Ag_2USe_4$, viewed down *a**.

however, the compounds are not isotypic. The only other compounds that adopt the $K_2Cu_2CeS_4$ structure type are $Na_2Cu_2ZrS_4$[30] and $K_2Cu_2ThS_4$.[31] However, the respective reduced cells of these three compounds and that of the current $Tl_2Ag_2USe_4$ differ and cannot be transformed into one another. The ionic radius of six-coordinate U^{4+} (0.89 Å)[32] is near that of Ce^{3+} (1.01 Å), and seven-coordinate Tl^{+} is slightly larger than K^{+} (1.59 Å vs 1.46 Å). The ionic radius of Ce^{3+} is given because $K_2Cu_2CeS_4$ has been formulated as $(K^{+})_2(Cu^{+})_2(Ce^{3+})(S^{2-})_3(S^{-})$. Therefore, the change in structure type may result from the presence of four-coordinate Ag^{+}, whose radius is approximately twice that of Cu^{+} (1.0 Å vs 0.6 Å).

The asymmetric unit of $Tl_2Ag_2USe_4$ contains the following atoms (and their site symmetries): U (2/*m*), Ag (*m*), Tl (*m*), Se(1) (*m*), and Se(2) (*m*). Each U atom is octahedrally coordinated by six Se atoms. Each Ag atom is tetrahedrally coordinated by four Se atoms, and each Tl atom is coordinated by seven Se atoms in a capped trigonal prismatic geometry. The structure of $Tl_2Ag_2USe_4$ consists of ${}^{2}_{\infty}[Ag_2USe_4{}^{2-}]$ layers separated by Tl^{+} cations. Within the ${}^{2}_{\infty}[Ag_2USe_4{}^{2-}]$ layer (Figure 4), each USe_6 octahedron shares edges with neighboring USe_6 octahedra in the [010] direction and also shares four edges and two corners with adjacent $AgSe_4$ tetrahedra. Every $AgSe_4$ tetrahedron shares one corner in the [100] direction, as well as two edges with USe_6 octahedra. The $AgSe_4$ tetrahedra also share corners in the [010] direction, as well as two edges with neighboring $AgSe_4$ tetrahedra. Within the ${}^{2}_{\infty}[Tl_2Se_4{}^{6-}]$ layer, each $TlSe_7$ trigonal prism shares three faces and four edges with adjacent $TlSe_7$ polyhedra. There are no Se−Se bonds in the structure. The shortest Se···Se interaction is 3.80 Å.

Table 4. Layered Quaternary Actinide Chalcogenides

compound(s)[a]	crystal system	space group	polyhedral packing[b]	reference
$AMAnQ_3$	orthorhombic	*Cmcm*	*oct tet oct tet*	2, 19, 31, 33, 35−38
$CsMUTe_5$	orthorhombic	*Pmma*	*oct btp btp oct*	39
$Cs_2Pd_3USe_6$	orthorhombic	*Fmmm*	*tp sp sp tp*	43
$K_3Cu_3Th_2S_7$	orthorhombic	*Pbcn*	*oct tet oct tet tet*	31
$K_2Cu_3US_5$	orthorhombic	*Cmcm*	*oct tet tet tet oct*	45
$Ba_2Cu_2US_5$	monoclinic	*C*2/*m*	*oct tet tet oct*	22
$Cs_2Hg_2USe_5$	monoclinic	*P*2/*n*	*oct tet tet oct*	44
$Tl_3Cu_4USe_6$	monoclinic	$P2_1/c$	*oct tet tet oct*	this work
$K_2Cu_2ThS_4$	monoclinic	*C*2/*m*	*oct tet tet oct*	31
$Tl_2Ag_2USe_4$	monoclinic	*C*2/*m*	*oct tet tet oct*	this work

[a] For the listed compound(s), A = alkali metal, An = actinide, M = transition metal, and Q = chalcogenide. [b] For the given representations of polyhedral packing, *btp* = bicapped trigonal prism, *oct* = octahedron, *sp* = square plane, *tet* = tetrahedron, and *tp* = trigonal prism.

Layered Quaternary Actinide Chalcogenides. Although there are examples of quaternary actinide chalcogenides with one-dimensional ($Cs_8Hf_5UTe_{30.6}$)[33] or three-dimensional ($K_6Cu_{12}U_2S_{15}$)[34] structures, the vast majority adopt two-dimensional layered structures (Table 4). For the purposes of this comparison, we will consider only compounds with an alkali metal (or Tl) or alkaline-earth metal, a transition metal, an actinide, and a chalcogen. The most common subset of this family of compounds is $AMAnQ_3$ (A = K, Rb, Cs; M = Cu, Ag, Au; An = Th, U, Np; Q = S, Se, Te);[2,19,31,33,35−38] these crystallize in space group *Cmcm* of the orthorhombic system in the $KCuZrS_3$ structure type.[25] This structure is particularly stable, as evidenced by the fact that it is the only one to display substitution on the alkali-metal/alkaline-earth metal, actinide, and chalcogen sites. It is one of two structure types, along with $CsMUTe_5$ (M = Ti, Zr),[39] also to exhibit variation on the transition-metal site. There are only single examples and no analogues of the other layered quaternary actinide chalcogenides.

The $KCuZrS_3$ structure can be derived from that of UI_3,[40] as previously discussed.[33] The UI_3 structure contains UI_8 bicapped trigonal prisms, with both tetrahedral and octahedral holes. Placing Fe into the empty octahedral sites and replacing I with S yields the structure of $FeUS_3$.[41,42] The addition of Cu into the vacant tetrahedral sites, the substitution of Zr for Fe, and the replacement of U with K gives the $KCuZrS_3$ structure type. The $AMUQ_3$ compounds in the $KCuZrS_3$ structure type feature two-dimensional ${}^{2}_{\infty}[MAnQ_3{}^{-}]$ layers stacked in the [010] direction, with alkali-metal cations intercalated between the layers. The layers contain alternating MQ_4 tetrahedra and AnQ_6 octahedra. The other layered quaternary actinide chalcogenides, with the exception of $CsMUTe_5$ (M = Ti, Zr) and $Cs_2Pd_3USe_6$,[43] present variations on this theme of MQ_4 and AnQ_6 packing within layers, separated by intercalated cations. All of the other examples either belong also to the orthorhombic system or descend in symmetry to the monoclinic system.

Note that there are four combinations of octahedral and tetrahedral packing in the layered quaternary actinide chalcogenides (Table 4). The first and simplest packing sequence is *oct tet oct tet*, as noted for the $AMUQ_3$ compounds. The second packing sequence is *oct tet tet oct*, as observed in five different structure types ($Ba_2Cu_2US_5$,[22] $Cs_2Hg_2USe_5$,[44] $Tl_3Cu_4USe_6$, $K_2Cu_2ThS_4$,[31] and $Tl_2Ag_2USe_4$). To move from $K_2Cu_2ThS_4$ and $Tl_2Ag_2USe_4$ to $Ba_2Cu_2US_5$, the alkali metal (or Tl) with an

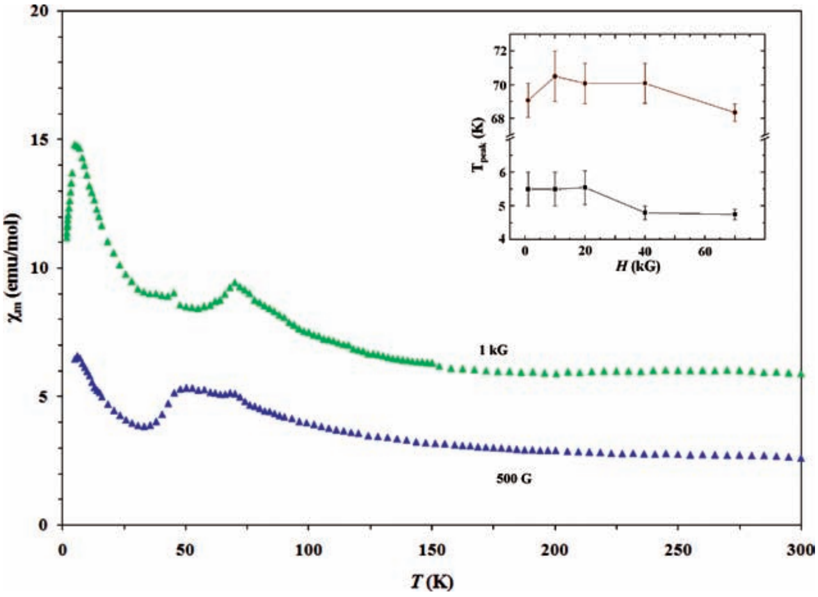

Figure 5. The magnetic susceptibility (χ_m) versus T for $Tl_3Cu_4USe_6$. The inset shows the field dependence of the peak temperatures.

oxidation state of +1 is replaced by a Ba^{2+} cation, necessitating an additional chalcogenide anion (Q^{2-}). To interchange between $Ba_2Cu_2US_5$ and $Cs_2Hg_2USe_5$, the Ba^{2+} cations are replaced by Cs^+ cations, and consequently the Cu^+ cations are replaced by Hg^{2+} cations to maintain charge balance. To move from $Cs_2Hg_2USe_5$ to $Tl_3Cu_4USe_6$, the two Hg^{2+} cations are isoelectronically substituted by four Cu^+ cations, and a Se^{2-} anion is inserted, which requires an additional charge of +2 to preserve charge balance. This is achieved by the addition of Tl^+ ($2Cs^+$ become $3Tl^+$) and the oxidation of U^{4+} in $Cs_2Hg_2USe_5$ to U^{5+} in $Tl_3Cu_4USe_6$.

The third packing sequence, *oct tet oct tet tet*, is found in $K_3Cu_3Th_2S_7$.[31] It is a combination of the previous two. The fourth combination of octahedral and tetrahedral packing is *oct tet tet tet oct*, as observed in $K_2Cu_3US_5$.[45] Two layered quaternary actinide chalcogenides do not obey this packing of octahedral AnQ_6 and tetrahedral MQ_4 units into layers separated by alkali metal (or Tl) or alkaline-earth metal cations. The first, $CsMUTe_5$ (M = Ti, Zr), features two-dimensional $^{2}_{\infty}[MUTe_5^{-}]$ layers stacking in the [010] direction. These layers contain MQ_6 octahedra and UTe_8 bicapped trigonal prisms, which pack in the sequence *oct btp btp oct*. The other compound is $Cs_2Pd_3USe_6$, with two-dimensional $^{2}_{\infty}[Pd_3USe_6^{2-}]$ layers in the [010] direction, made up of square planar $PdSe_4$ units and USe_6 trigonal prisms packing in the sequence *tp sp sp tp*.

Except for $Cs_2Pd_3USe_6$ and $Tl_3Cu_4USe_6$, all of the other layered quaternary actinide chalcogenides feature edge-sharing of the AnQ_6 (or AnQ_8) polyhedra with one another in the direction perpendicular to the packing with the MQ_4 (or MQ_6) polyhedra. The $^{2}_{\infty}[Pd_3USe_6^{2-}]$ layer of $Cs_2Pd_3USe_6$ contains USe_6 trigonal prisms separated from one another by hexagonal Pd_6Se_{12} rings. Within the $^{2}_{\infty}[Cu_4USe_6^{3-}]$ layer of $Tl_3Cu_4USe_6$, each USe_6 octahedron is completely isolated from all surrounding USe_6 octahedra by intervening $CuSe_4$ tetrahedra.

Magnetic Susceptibility of $Tl_3Cu_4USe_6$. Figure 5 displays the magnetic behavior of $Tl_3Cu_4USe_6$. The overall magnetic susceptibility increases upon cooling, with two prominent peaks around 5 and 70 K. The inset shows the field dependence of peak positions. The peaks are robust and are nearly independent of applied magnetic field strengths and ZFC and FC conditions. The origin of the two peaks is currently unknown. The shape of the peaks is more cusp-like than the broad maxima usually originating from the crystal electric field (CEF) effect. The Weiss temperature estimated from the modified Curie–Weiss fitting (see below) is small but positive, indicating ferromagnetic interaction. It is possible that the origin of the 70 K peak is similar to that of another U^{5+} chalcogenide, $K_2Cu_3US_5$,[45] where a maximum in the magnetic susceptibility around 94 K was ascribed to a magnetic or structural phase change, possibly coupled to a Cu–U charge transfer. This possibility is supported by the robustness of the 70 K peaks and the fact that the USe_6 octaheda are well separated by $CuSe_4$ tetrahedra.

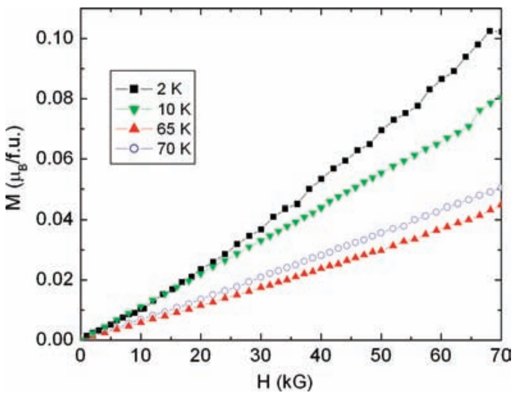

Figure 6. Isothermal magnetization measurements for $Tl_3Cu_4USe_6$ at 2, 10, 65, and 70 K.

To apply the modified Curie–Weiss law ($\chi_m = \chi_0 + C/(T - \theta_p)$), in the temperature range above 70 K, diamagnetic contributions from both the core electrons and sample holder were subtracted from the magnetic susceptibility data. The fitting results give temperature-independent terms χ_0 equal to 4.30×10^{-3} emu mol^{-1} (500 G) and 4.38×10^{-3} emu mol^{-1} (1 kG). The positive χ_0 can

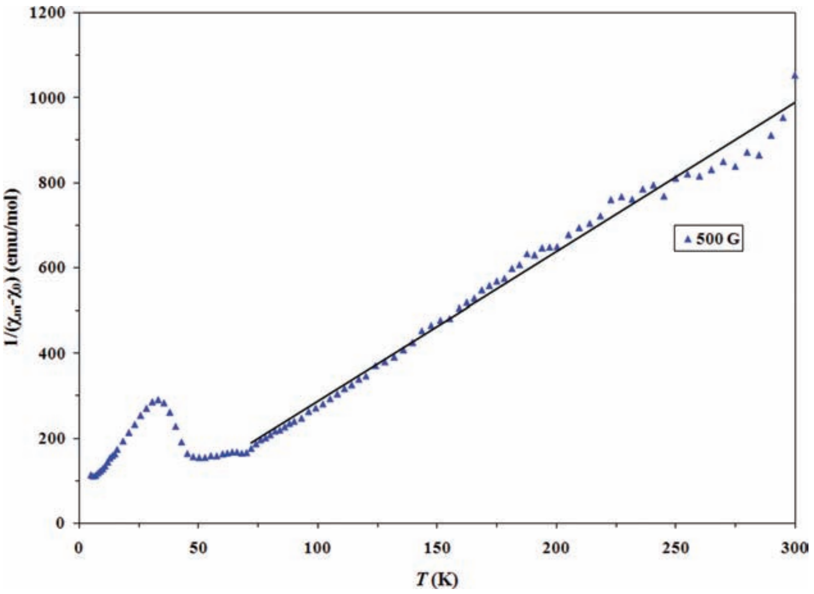

Figure 7. Plot of $1/(\chi_m - \chi_0)$ versus T for $Tl_3Cu_4USe_6$, showing a straight-line fit to the modified Curie−Weiss law.

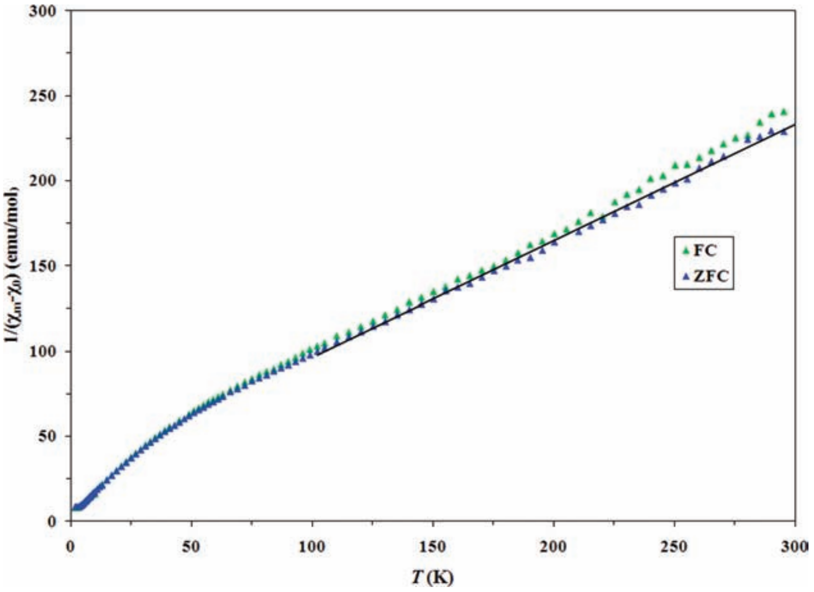

Figure 8. Plot of $1/(\chi_m - \chi_0)$ versus T for $Tl_2Ag_2USe_4$, showing a straight-line fit to the modified Curie−Weiss law.

be attributed to Pauli paramagnetism from conduction electrons or ferromagnetic impurities. Ferromagnetic impurities are less likely considering the synthetic procedure and the isothermal magnetization data shown in Figure 6. The existence of conduction electrons should be verified by further measurements.

The resulting plot of $1/(\chi_m - \chi_0)$ versus T (H = 500 G) for $Tl_3Cu_4USe_6$ is shown in Figure 7. In the temperature range 72−300 K, the fit to the data results in values of 0.289 emu K mol^{-1} and 18(2) K for the Curie constant C and the Weiss constant θ_p, respectively. The effective magnetic moment, μ_{eff}, as calculated from the equation $\mu_{eff} = (7.997C)^{1/2}\ \mu_B$,[46] is 1.58(1) μ_B. If $Tl_3Cu_4USe_6$ contains U^{4+} and only one Cu^{2+} cation (as well as three Cu^+ cations for charge balance), the calculated effective magnetic moment is 3.98 μ_B. However, if $Tl_3Cu_4USe_6$ contains only U^{5+} and diamagnetic Cu^+, the calculated effective magnetic moment is due entirely to the free-ion moment for U^{5+} (2.54 μ_B for the Russell−Saunders coupling scheme and 1.73 μ_B for the spin-only model).[47] On the assumption that only U possesses a magnetic moment (see below), the reduced effective magnetic moment can be due to CEF effects with energy level splittings comparable to the measured temperatures. A number of other U^{5+} compounds have effective magnetic moments of less than 2.0 μ_B, including UCl_5 (1.26 μ_B),[48] UO_2Br (1.76 μ_B),[49] $LiUO_3$ (1.81 μ_B),[48] and $K(UO)Si_2O_6$ (1.32 μ_B).[50]

Magnetic Susceptibility of $Tl_2Ag_2USe_4$. The magnetic behavior of $Tl_2Ag_2USe_4$ (Figure 8) is significantly less complex than that of $Tl_3Cu_4USe_6$. Upon application of the modified Curie−Weiss law, the magnetic susceptibility data for $Tl_2Ag_2USe_4$ yield a temperature-independent term χ_0 equal to $-4.8(2) \times 10^{-3}$ emu mol^{-1}. This value represents the

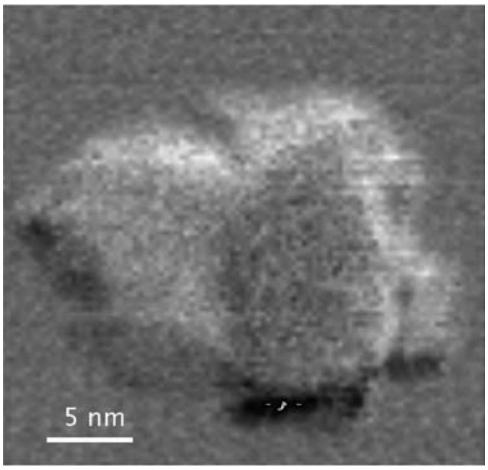

Figure 9. A normal contrast image collected from a particle obtained from powdered $Tl_3Cu_4USe_6$ with a photon energy of 737 eV.

Table 5. XANES Transition Maxima (eV)

Se compound	Se $2p_{3/2}$ (L_3) [A]	feature [B]	Se $2p_{1/2}$ (L_2) [C]	feature [D]
USe_3	1436.1	yes	1477.2	yes
$Tl_3Cu_4USe_6$	1436.4	yes	1479.1	yes
β−USe_2	1437.7		1478.5	yes
$RbAuUSe_3$	1436.6	yes		yes
Se (elemental)	1435.3	yes	1476.1	yes
Cu compound	Cu $2p_{3/2}$ (L_3)			Cu $2p_{1/2}$ (L_2)
CuO	931.6	939.9		951.4
$Tl_3Cu_4USe_6$	932.7; 934.7	937.7	∼946	∼953
CuSe	931.5	933.8	938.4	951.1; 953.5
Cu_2O	933.7	938.3	946.7	953.5
U compound		U $4d_{5/2}$ (N_5)		U $4d_{3/2}$ (N_4)
$(UO_2)_4O(OH)_6 \cdot 6H_2O$		738.4		779.8
$Tl_3Cu_4USe_6$		737.0		778.4
β-USe_2		736.6		777.8
$RbAuUSe_3$		736.9		778.1

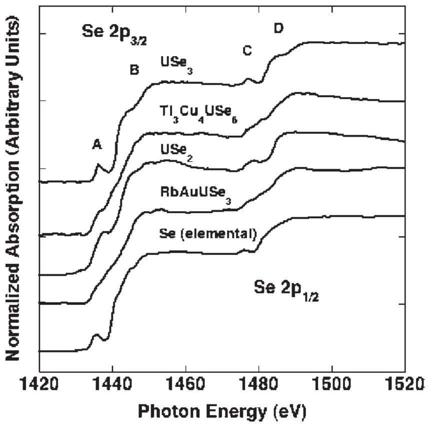

Figure 10. Selenium $2p_{3/2,1/2}$ near-edge spectra obtained from particles of USe_3, $Tl_3Cu_4USe_6$, β-USe_2, $RbAuUSe_3$, and elemental Se (top to bottom, respectively). The spectra have been normalized to unity at 1520 eV.

diamagnetic contributions from both the core electrons and the sample holder. The resulting plot of $1/(\chi_m - \chi_0)$ versus T for $Tl_2Ag_2USe_4$ is shown in Figure 8. Above 100 K, the modified Curie−Weiss fit to the data results in values of 1.46(1) emu K mol^{-1} and −41(1) K for the Curie constant C and the Weiss constant θ_p, respectively. The negative Weiss constant (−41(1) K) indicates antiferromagnetic interaction, and the effective magnetic moment, μ_{eff}, is 3.4(1) μ_B. This effective magnetic moment is comparable to the values of the free-ion moments for U^{3+} (3.62 μ_B) and U^{4+} (3.58 μ_B), as calculated from L−S coupling.[47] Some other U^{4+} selenides exhibit similar effective magnetic moments, including $Cu_2U_6Se_{13}$ (3.27 μ_B/U),[51] $Rh_2U_6Se_{15.5}$ (3.41 μ_B/U),[52] $Ir_2U_6Se_{15.5}$ (3.43 μ_B/U),[52] and $KCuUSe_3$ (3.65 μ_B).[36] The linear behavior of the inverse magnetic susceptibility deviates significantly at low temperatures, which is often ascribed to the CEF effect of the 5f electrons.

Scanning Transmission X-Ray Microscopy (STXM) Spectromicroscopy. Figure 9 shows a normal contrast image of the $Tl_3Cu_4USe_6$ particle collected at 737 eV from which XANES spectra were recorded. The X-ray image shows that the particle is uniform in composition on the nanometer scale. A summary of the XANES peak positions is given in Table 5.

Selenium XANES. The Se $2p_{3/2,1/2}$ near-edge spectra recorded from USe_3, $Tl_3Cu_4USe_6$, β-USe_2, $RbAuUSe_3$, and elemental Se are shown in Figure 10. All of the Se XANES spectra have had linear backgrounds subtracted, have been five-point smoothed, and have been normalized to the signal at 1520 eV. The Se $2p_{3/2,1/2}$ transitions indicated in Figure 10 occur at about 1433.9 and 1474.3 eV.[53] XANES spectroscopy at the 2p edge has not been employed extensively to determine oxidation states of Se-containing materials; however, there have been some investigations.[54,55] The β-USe_2 and $RbAuUSe_3$ materials, both of which contain only discrete Se^{2-} units, provide reference spectra. The USe_3 spectrum is representative of a mixture of discrete Se^{2-} anions and diselenide ($Se_2{}^{2-}$) units.

The Se L-edge XANES spectrum of $Tl_3Cu_4USe_6$ shown in Figure 10 has distinguishable features centered at about 1436.4 eV (A), a very broad feature extending between ∼1440 and 1460 eV (B), a distinct peak at 1479.1 eV (C), and a final broad feature appearing at 1481.3−1500 eV (D). The β-USe_2 Se 2p spectrum is similar to that of $Tl_3Cu_4USe_6$, with the exception of more well-resolved features at A and C. The XANES spectrum of the $RbAuUSe_3$ reference for Se^{2-} has a small feature at 1436.6 eV, a broad, smooth feature from about 1400 to 1460 eV, no sharp feature in location C, and a final broad feature starting at 1473.9 eV and extending out to 1500 eV. The $RbAuUSe_3$ reference spectrum is nearly identical to that of $Tl_3Cu_4USe_6$. The reference spectrum for mixed Se speciation, USe_3, has features at 1436.1 eV, a broad feature at ∼1440 eV, a notable peak at 1477.2 eV, and another broad feature starting at 1480 eV and extending to 1500 eV.

The $Tl_3Cu_4USe_6$ Se 2p spectrum does not exhibit a prominent feature at A and has differences in line shape near B compared to the spectrum of USe_3. Moreover, there is no direct evidence for the existence of chain or polymeric Se bonding characteristics based on the spectra of known reference materials.[55] That the Se 2p spectrum from $Tl_3Cu_4USe_6$ is nearly the same as the spectra obtained from β-USe_2 and $RbAuUSe_3$ is strong evidence that it contains only Se^{2-} units.

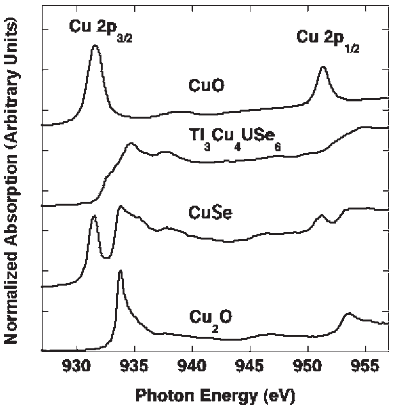

Figure 11. Copper $2p_{3/2,1/2}$ near-edge spectra obtained from particles of CuO, $Tl_3Cu_4USe_6$, CuSe, and Cu_2O (top to bottom, respectively). The spectra have been normalized to unity at the Cu $2p_{3/2}$ feature.

Copper XANES. The Cu 2p-edge XANES spectra from CuO, $Tl_3Cu_4USe_6$, CuSe, and Cu_2O are shown in Figure 11. All of the spectra in Figure 11 have had linear backgrounds subtracted and have been normalized to unity at the Cu $2p_{3/2}$ feature for relative line shape comparison. Monovalent, formally Cu^+ species yield Cu 2p spectra with a leading Cu $2p_{3/2}$ feature at 932.5−933.5 eV with additional material-specific features that may appear before 940 eV and followed by the Cu $2p_{1/2}$ spin−orbit partner at about 953.5 eV.[56] Somewhat similar to monovalent Cu spectral features, metallic Cu shows simultaneous features at approximately 934.0 and 937.5 eV. In the Cu 2p spectra shown in Figure 11, there is no evidence for the presence of metallic Cu. Spectra of divalent, formally Cu^{2+} species show a well-defined, intense singular Cu $2p_{3/2}$ peak around 931.0 eV that can exhibit small peaks on the high energy side depending on the material and are accompanied by the spin−orbit component at an energy ~20 eV higher, as shown by CuO in Figure 11. The Cu^{2+} Cu $2p_{3/2}$ peak is about 25 times more intense than the same feature from Cu^+ materials.[57] The spectra of Cu species that are formally trivalent, Cu^{3+}, are characterized by Cu $2p_{3/2}$ peaks at about 934 eV with the corresponding spin−orbit peak 20 eV higher.[58] Cu^{3+} spectra also show a small, broad feature at 941 eV. The Cu 2p spectra of Cu^{3+} materials sometimes show components of Cu^{2+} spectra resulting from impurities or destabilization under vacuum conditions. A detailed summary of Cu 2p XANES spectroscopy is available.[57]

Prior to the interpretation of the Cu 2p XANES from $Tl_3Cu_4USe_6$, it is important to verify and understand the XANES spectra from the monovalent reference materials used in this investigation, Cu_2O and CuSe. Note that CuSe is a compound of Cu^+ rather than of Cu^{2+}.[59] In all spectra collected here, the Cu $2p_{1/2}$ peak manifold structure reflects that of the corresponding Cu $2p_{3/2}$ manifold but is broadened by the Cu $2p_{3/2}$ continua and other contributions.[60] The prototypical Cu 2p XANES spectrum of the reference material Cu_2O has been collected and interpreted in several previous investigations.[56] In Figure 11, the intensity of the Cu $2p_{3/2}$ feature at 933.7 eV in the Cu_2O spectrum collected here is greater (~3×) relative to that from the corresponding lead Cu $2p_{3/2}$ feature in CuSe and $Tl_3Cu_4USe_6$ before normalization. There is also a well-developed $2p_{1/2}$ feature at 953.5 eV that yields a spin−orbit split of 19.8 eV. Thus, the Cu_2O spectrum corresponds nicely to those recorded previously with the unusual intensity of the Cu^+ $2p_{3/2}$ peak attributed to a structure in which Cu is linearly coordinated to two oxygen nearest neighbors.[61]

The spectrum of CuSe shown in Figure 11 has two prominent features in the Cu $2p_{3/2}$ region. The first peak at 931.5 eV we attribute to Cu^{2+} impurities, given that the intensities of Cu^{2+} features are much greater than those of Cu^+. The second peak at 933.8 eV is characteristic of a normal Cu^+ material, in energy being comparable to that of Cu_2O with a much lower intensity for reasons previously mentioned. As observed in general for monovalent Cu^+ materials, the exact energy of the primary Cu $2p_{3/2}$ Cu^+ feature as well as any additional fine structure on the high energy tail of the primary peak are material-specific, and thus in CuSe these vary slightly from those of other Cu^+ species, including Cu_2O.[56] In CuSe, there is a broad feature originating at ~938 eV stretching to 940 eV that is also associated with Cu^+ species, and upon close inspection this feature can be found in the Cu_2O spectrum. A faint feature centered at 946.0 eV is also apparent in the CuSe spectrum; a similar feature is present in the Cu_2O spectrum. The fine features on the higher energy side of the primary Cu^+ Cu $2p_{3/2}$ peak in the CuSe spectrum are more apparent than those from Cu_2O, because of the unusually high intensity of the primary Cu^+ Cu $2p_{3/2}$ peak in the Cu_2O spectrum and the method used to normalize the spectra for presentation in Figure 11.

Turning now to $Tl_3Cu_4USe_6$, we show its Cu 2p XANES spectrum in Figure 11. Upon initial inspection it does not closely resemble spectra of the Cu reference materials. An important observation is that the intensity of its overall XANES spectrum is similar to that from CuSe rather than those from the two oxides Cu_2O (Cu^+) and CuO (Cu^{2+}). The most notable feature is the absence of sharp transitions in the $Tl_3Cu_4USe_6$ spectrum that would be expected for a Cu^{2+} species. Instead, the $Tl_3Cu_4USe_6$ $2p_{3/2}$ region is composed of three broad, distinguishable, and convoluted features. The first feature resides on the low-energy shoulder of the second and most prominent peak at 934.7 eV. The first feature, which does not correspond to a peak found in either reference spectrum, precedes by 1 eV the onset of the energy at which a Cu^+ peak would be expected. The main $Tl_3Cu_4USe_6$ peak resides 1 eV toward higher energy from those found in the reference materials. The third $Tl_3Cu_4USe_6$ feature corresponds to similar features at the same energies observed in the reference materials, albeit the intensity of the feature in Cu_2O is obscured by the overall intensity of the main line. The region from 940 to 950 eV has an uneven background, and no features are resolved with certainty. Lastly, the $Tl_3Cu_4USe_6$ Cu $2p_{1/2}$ manifold shows no distinct structure other than replication of the overall shape of the Cu $2p_{3/2}$ region with less amplitude and resolution.

To summarize, the overall intensity of the Cu 2p XANES spectrum gives strong evidence for a Cu^+ species. Importantly, there is no signature Cu^{2+} transition that occurs at a well-defined energy with a substantial cross-section. The two convoluted lead peaks in the $Tl_3Cu_4USe_6$ $2p_{3/2}$ region make the overall transition appear broad, possibly because there are four crystallographically independent Cu atoms in the structure. However, these lead peaks are centered around Cu^+ transition energies and are comparable in general profile to the same feature in the CuSe spectrum. Similar spectra for monovalent species have been recorded for complex tetrahedrites.[62] Trivalent Cu^{3+} would exhibit features at about 934 eV accompanied by another at 941 eV, and neither is observed. We conclude that the formal oxidation state of Cu in $Tl_3Cu_4USe_6$ is +1.

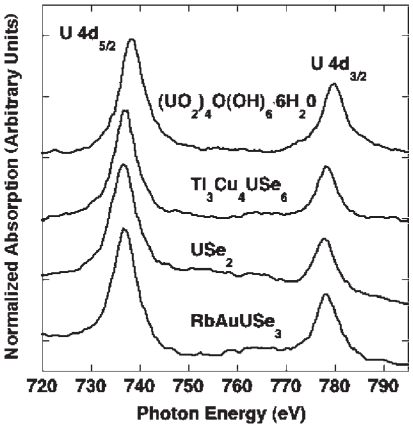

Figure 12. Uranium $4d_{5/2,3/2}$ absorption spectrum collected from particles of $(UO_2)_4O(OH)_6 \cdot 6H_2O$ (Schoepite), $Tl_3Cu_4USe_6$, β-USe_2, and $RbAuUSe_3$ (top to bottom, respectively) with the spectra normalized to the U $4d_{5/2}$ feature.

Uranium XANES. The U 4d-edge XANES spectra from $Tl_3Cu_4USe_6$ and reference materials are shown in Figure 12. The U spectrum from $Tl_3Cu_4USe_6$ has not had the background subtracted, whereas the other three U spectra have had linear backgrounds removed. All U spectra have been three-point smoothed and normalized to the U $4d_{5/2}$ feature. The most prominent features in Figure 12 are the U $4d_{5/2}$ and U $4d_{3/2}$ white-line transitions. These transitions from the U 4d orbitals primarily probe unoccupied states with U 5f character. The charge state shift of the U $4d_{5/2}$ transition can be used to assign an effective oxidation state based on its energy.[14,15,63] The broad feature centered at about 760 eV between white lines has been observed previously in U spectra but has yet to be assigned. However, the broad features in the $RbAuUSe_3$ spectrum beginning just after 760 eV and tailing into the U $4d_{3/2}$ features are absorption from the Au constituent at ~763 eV (Au 4s).

The maxima of the U $4d_{5/2}$ and U $4d_{3/2}$ transitions for $Tl_3Cu_4USe_6$ are located at 737.0 and 778.4 eV, respectively. The 4d transition energies from $Tl_3Cu_4USe_6$ correspond to U 4d-edge energies obtained from similar constituent-containing and well-characterized U^{4+} reference materials. These transitions are comparable to those in $RbAuUSe_3$ at 736.9 and 778.1 eV and those in β-USe_2 at 736.6 and 777.8 eV.[55] A dissimilar U^{4+} material, namely, the coordination complex $[U(BBP)_3]Cl_4$ (BBP = 2,6-bis(2-benzimidazyl)pyridine), has U 4d-edge transitions at 736.9 and 778.4 eV. More traditional U^{4+} materials such as UCl_4 and UO_2 have $4d_{5/2}$ transitions at 737.1 and 737.5 eV.[64] The $Tl_3Cu_4USe_6$ $4d_{5/2}$ transition energies lie well above the transition energies of 736.6 and 736.7 eV determined for the U^{3+} complexes $[U(BBP)_3]I_3$ and $(CpSiMe_3)_3U$-$AlCp^*$, respectively.[14,65] The lower energy charge state boundary is set by U metal with a U $4d_{5/2}$ transition at 736.4 eV. The U^{6+} $4d_{5/2}$ charge state energies for uranyl species start at about 738.4 eV, as shown by the $(UO_2)_4O(OH)_6 \cdot 6H_2O$ (Schoepite) spectrum in Figure 12, whereas there have yet to be studies of a U^{6+} uranate.[64]

The charge state of U in $Tl_3Cu_4USe_6$ is definitely not +3, nor is it +6. The U $4d_{5/2}$ transition energy in $Tl_3Cu_4USe_6$ is toward the upper energy range of U^{4+} materials of this class and that anticipated for possible U^{5+} species, such as $K_2Cu_3US_5$.[45] Unfortunately, we were unable to collect reproducible data from $K_2Cu_3US_5$ owing to the extremely small amount of single crystals that could be prepared.

The branching ratio ($4d_{5/2}/4d_{3/2}$) derived from the peak intensities of $Tl_3Cu_4USe_6$ is similar to those observed from β-USe_2, BBP complexes, and $RbAuUSe_3$ but different from those observed for uranyl U^{6+} materials (see Schoepite spectrum). The energy position of the $Tl_3Cu_4USe_6$ U $4d_{5/2}$ transition effectively rules out the U oxidation states of +6 and those less than +4. However, the current U $4d_{5/2}$-edge XANES spectra do not enable us to assign an exact charge state of U in $Tl_3Cu_4USe_6$, though they are consistent with U^{4+} and possibly U^{5+} species.

Formal Oxidation States. We will first consider $Tl_2Ag_2USe_4$. Because there are no Se−Se bonds in the structure, the formal oxidation states of Tl, Ag, U, and Se may be assigned as +1, +1, +4, and −2, respectively. An oxidation state of +4 for U is consistent with the magnetic data presented above. The U−Se distances of 2.853(3) and 2.881(1) Å (Table 3) are near those of 2.8715(4) and 2.8723(5) Å in $CsAgUSe_3$,[2] which also contains octahedral U^{4+}. The Ag−Se interatomic distances of 2.638(2)−2.799(2) Å in $Tl_2Ag_2USe_4$ are within the range of those of 2.585(1)−2.954(1) Å for tetrahedral Ag^+ in $CsAg_5Se_3$.[66] The Tl···Se distances of 3.120(2)−3.618(2) Å are within the range of 3.024(3)−3.849(3) Å found in $Tl_4Nb_2Se_{11}$.[67] There are short Ag···Ag distances (2.904(2) Å) in $Tl_2Ag_2USe_4$, which are only slightly longer than the Ag···Ag distances observed in Ag metal (2.88 Å),[3] and significantly less than the van der Waals diameter (3.44 Å).[68] These short Ag···Ag distances are indicative of d^{10}−d^{10} interactions.[69] Examples of other solid-state Ag chalcogenides that display d^{10}−d^{10} interactions include $CsAg_3S_2$,[70] $K_2Ag_4Se_3$,[71] and $CsAg_5Se_3$.[66]

Bond valence analysis[72] provides an empirical means of assigning formal oxidation states. Because it is based on data from interatomic distances, we would expect it to provide results consistent with the arguments above. Indeed it does, as the Bond Valence Calculator[73] yields the following oxidation states for $Tl_2Ag_2USe_4$: U, 3.60; Ag, 1.24; and Tl, 1.44.

We turn now to crystallographic evidence that bears on the question of the formal oxidation states of the metals in $Tl_3Cu_4USe_6$. Because there are no Se−Se bonds in the structure of $Tl_3Cu_4USe_6$, each Se atom can be considered a discrete Se^{2-} anion. Although Tl can be either +1 or +3, it is overwhelmingly found as +1 (analogous to alkali-metal cations) in ternary and quaternary chalcogenide systems. The Tl···Se distances of 2.990(2)−3.670(2) Å (Table 2) are consistent with those of 3.000(6)−3.787(7) Å found for Tl^+ in Tl_4SiSe_4.[74] Thus, the combined formal oxidation states of four Cu atoms and one U atom must be +9 in $Tl_3Cu_4USe_6$ in order to achieve charge balance. Possible formal oxidation states of Cu are +1 and +2, although +2 is unknown in chalcogenides, and its presence would be inconsistent with the XANES results. Likely formal oxidation states of U are +4 and +5, as supported by the XANES results. Moreover, U^{3+} rarely occurs and U^{6+} is unknown in chalcogenides, and neither is consistent with the XANES results. The limited number of U^{3+} chalcogenide compounds includes UTe_2,[75] U_3S_5,[76] U_2Q_3 (Q = S, Se, Te),[77−79] $ScUS_3$,[80] and ScU_3S_6.[81] The only known uranium chalcogenide that may contain U^{6+} is $A_6Cu_{12}U_2S_{15}$ (A = K, Rb, Cs),[34,82] which has previously been hypothesized to contain U^{5+} and S^- but may alternatively contain U^{6+}.

The Cu−Se interatomic distances in $Tl_3Cu_4USe_6$ of 2.427(2)−2.669(2) Å (Table 2) are comparable, though slightly longer than those found in $CsCuUSe_3$ (2.458(1) and 2.526(2) Å),[37] which contains Cu^+. Because the ionic radius of Cu^{2+} (0.57 Å) is smaller than that of Cu^+ (0.6 Å),[32] the Cu−Se distances would in fact be shorter if Cu^{2+} were present, which is not the case.

The U−Se interatomic distances range from 2.725(2) to 2.850(2) Å in $Tl_3Cu_4USe_6$, which are shorter than those found for other USe_6 octahedra in U^{4+} compounds. For comparison, the U−Se interatomic distances in $CsAgUSe_3$[2] are 2.8715(4)−2.8723(5) Å, and those in $Cs_2Hg_2USe_5$[44] are 2.872(1)−2.902(1) Å. Because the ionic radius of six-coordinate U decreases upon going from U^{4+} to U^{5+} (0.89 Å vs 0.76 Å),[32] interatomic distances should decrease accordingly. Unfortunately, there are no known U^{5+} selenides in the literature for comparison. However, this expected decrease is found for compounds with US_6 octahedra, where the U−S interatomic distances decrease from 2.714(1)−2.7165(9) Å in $KCuUS_3$,[2] which contains U^{4+}, to 2.587(1)−2.6827(9) Å in $K_2Cu_3US_5$,[45] which contains U^{5+}.

Similar to $Tl_2Ag_2USe_4$, $Tl_3Cu_4USe_6$ features short Cu···Cu distances, which range from 2.571(3) to 2.654(3) Å (Table 3). These distances are only slightly longer than the Cu···Cu distances observed in Cu metal (2.56 Å)[3] and significantly less than the van der Waals diameter (2.8 Å).[68] Short Cu···Cu distances, such as those observed in $Tl_3Cu_4USe_6$, are indicative of $d^{10}-d^{10}$ interactions.[69] Such interactions have been observed in a number of other solid-state Cu chalcogenides, including $Na_2Cu_4S_3$,[83] $Cs_2Cu_5Se_4$,[84] $Cs_3Cu_8Se_6$,[85] and $Tl_5Cu_{14}Se_{10}$.[86] Note that $d^{10}-d^{10}$ interactions are absent in Cu^{2+} compounds. Thus, their presence in $Tl_3Cu_4USe_6$ is further support for Cu^+ rather than Cu^{2+} in the compound. The only other U^{5+} solid-state chalcogenide, $K_2Cu_3US_5$,[45] also exhibits short Cu···Cu distances (2.7093(5) Å).

Once again, bond valence analysis[72] supports these formal oxidation states of +1 for Cu and +5 for U. The BondValence function in PLATON[87] provides the following oxidation states in $Tl_3Cu_4USe_6$: U(1), 4.85; U(2), 4.77; Cu(1), 0.83; Cu(2), 0.78; Cu(3), 0.85; and Cu(4), 0.77. Thus, the magnetic measurements, the XANES measurements, and the crystallographic results provide consistent evidence for a formal oxidation state of +5 for U in $Tl_3Cu_4USe_6$.

Speculation on the Syntheses of U^{5+} Compounds. U^{5+} systems are of particular interest because of their $5f^1$ electronic configuration. The study of such systems allows for a better understanding of what contribution the 5f orbitals make to structure, bonding, and physical properties. Recent work in uranium organometallic chemistry has demonstrated the use of Cu^+ halides as agents for the oxidation of U^{4+} complexes to U^{5+} complexes.[88,89] The present compound, $Tl_3Cu_4USe_6$, was synthesized from U, Cu, Se, and TlCl; the solid-state U^{5+} chalcogenide, $K_2Cu_3US_5$,[45] was synthesized from K_2S, UCl_4, S, and CuCl. Perhaps the current synthesis of $Tl_3Cu_4USe_6$ is generating CuCl and UCl_4 *in situ* via the reaction of TlCl with Cu and U. We speculate that syntheses that make use of U, Cu, and halide salts may provide additional U^{5+} compounds.

■ ASSOCIATED CONTENT

Ⓢ Supporting Information. Crystallographic files in CIF format for $Tl_3Cu_4USe_6$ and $Tl_2Ag_2USe_4$ and additional details on the XANES measurements. This material is available free of charge via the Internet at http://pubs.acs.org.

■ AUTHOR INFORMATION

Corresponding Author

*E-mail: ibers@chem.northwestern.edu.

■ ACKNOWLEDGMENT

The research at Northwestern University was kindly supported by the U.S. Department of Energy, Basic Energy Sciences, Chemical Sciences, Biosciences, and Geosciences Division and Division of Materials Sciences and Engineering Grant ER-15522. Magnetic measurements for $Tl_2Ag_2USe_4$ were made at the Materials Research Science and Engineering Center, Magnet and Low Temperature Facility, supported by the National Science Foundation (DMR05-20513). Magnetic measurements for $Tl_3Cu_4USe_6$ were made at the National High Magnetic Field Laboratory, supported by the National Science Foundation (DMR-0654118) and by the State of Florida. Parts of this work (R.C., P.-A.G., S.G.M., T.T., D.K.S.) and the ALS were supported by the Director, Office of Science, Office of Basic Energy Sciences and the Division of Chemical Sciences, Geosciences, and Biosciences of the U.S. Department of Energy at LBNL under Contract No. DE-AC02-05CH11231. Parts of this work were also supported by the Glenn T. Seaborg Institute postdoctoral fellowship program (S.G.M.) and the Division of Chemical Sciences, Geosciences, and Biosciences, Office of Basic Energy Sciences, U.S. Department of Energy, under the Heavy Elements Chemistry Program at LANL (S.G.M., S.A.K.). LANL is operated by the Los Alamos National Security, LLC, for the National Nuclear Security Administration of the U.S. Department of Energy under Contract DE-AC52-06NA25396.

■ REFERENCES

(1) Narducci, A. A.; Ibers, J. A. *Chem. Mater.* **1998**, *10*, 2811–2823.

(2) Yao, J.; Wells, D. M.; Chan, G. H.; Zeng, H.-Y.; Ellis, D. E.; Van Duyne, R. P.; Ibers, J. A. *Inorg. Chem.* **2008**, *47*, 6873–6879.

(3) Greenwood, N. N.; Earnshaw, A. *Chemistry of the Elements*; Pergamon Press: New York, 1989.

(4) Allred, A. L. *J. Inorg. Nucl. Chem.* **1961**, *17*, 215–221.

(5) Bugaris, D. E.; Wells, D. M.; Yao, J.; Skanthakumar, S.; Haire, R. G.; Soderholm, L.; Ibers, J. A. *Inorg. Chem.* **2010**, *49*, 8381–8388.

(6) Tougait, O.; Daoudi, A.; Potel, M.; Noël, H. *Mater. Res. Bull.* **1997**, *32*, 1239–1245.

(7) Haneveld, A. J. K.; Jellinek, F. *J. Less-Common Met.* **1969**, *18*, 123–129.

(8) *APEX2*, version 2009.5-1; *SAINT*, version 7.34a; Bruker Analytical X-Ray Instruments, Inc.: Madison, WI, 2009.

(9) Sheldrick, G. M. *SADABS*; Department of Structural Chemistry, University of Göttingen: Göttingen, Germany, 2008.

(10) Sheldrick, G. M. *Acta Crystallogr., Sect. A* **2008**, *64*, 112–122.

(11) Gelato, L. M.; Parthé, E. *J. Appl. Crystallogr.* **1987**, *20*, 139–143.

(12) Bluhm, H.; Andersson, K.; Araki, T.; Benzerara, K.; Brown, G. E.; Dynes, J. J.; Ghosal, S.; Gilles, M. K.; Hansen, H.-C.; Hemminger, J. C.; Hitchcock, A. P.; Ketteler, G.; Kilcoyne, A. L. D.; Kneedler, E.; Lawrence, J. R.; Leppard, G. G.; Majzlam, J.; Mun, B. S.; Myneni, S. C. B.; Nilsson, A.; Ogasawara, H.; Ogletree, D. F.; Pecher, K.; Salmeron, M.; Shuh, D. K.; Tonner, B.; Tyliszczak, T.; Warwick, T.; Yoon, T. H. *J. Electron Spectrosc. Relat. Phenom.* **2006**, *150*, 86–104.

(13) Janousch, M.; Copping, R.; Tyliszczak, T.; Castro-Rodriguez, I.; Shuh, D. K. *Mater. Res. Soc. Symp. Proc.* **2008**, *1104*, 165–170.

(14) Minasian, S. G.; Krinsky, J. L.; Rinehart, J. D.; Copping, R.; Tyliszczak, T.; Janousch, M.; Shuh, D. K.; Arnold, J. *J. Am. Chem. Soc.* **2009**, *131*, 13767–13783.

(15) Stöhr, J. *NEXAFS Spectroscopy*, 2nd ed.; Springer-Verlag: Berlin, 2003.

(16) Hitchcock, A. P. *aXis*, version 17-Sep-08; McMaster University: Hamilton, ON, Canada, 2008.

(17) Noël, H.; Potel, M.; Troc, R.; Shlyk, L. *J. Solid State Chem.* **1996**, *126*, 22–26.

(18) Kwak, J.-E.; Gray, D. L.; Yun, H.; Ibers, J. A. *Acta Crystallogr., Sect. E* **2006**, *62*, i86–i87.

(19) Bugaris, D. E.; Ibers, J. A. *J. Solid State Chem.* **2009**, *182*, 2587–2590.

(20) Tougait, O.; Potel, M.; Noël, H. *J. Solid State Chem.* **1998**, *139*, 356–361.

(21) Huang, F. Q.; Ibers, J. A. *J. Solid State Chem.* **2001**, *159*, 186–190.

(22) Zeng, H.-Y; Yao, J.; Ibers, J. A. *J. Solid State Chem.* **2008**, *181* 552–555.

(23) Huang, F. Q.; Choe, W.; Lee, S.; Chu, J. S. *Chem. Mater.* **1998**, *10*, 1320–1326.

(24) Sunshine, S. A.; Kang, D.; Ibers, J. A. *J. Am. Chem. Soc.* **1987**, *109*, 6202–6204.

(25) Mansuetto, M. F.; Keane, P. M.; Ibers, J. A. *J. Solid State Chem.* **1992**, *101*, 257–264.

(26) McGuire, M. A.; Reynolds, T. K.; DiSalvo, F. J. *Chem. Mater.* **2005**, *17*, 2875–2884.

(27) Pell, M. A.; Ibers, J. A. *J. Alloys Compd.* **1996**, *240*, 37–41.

(28) Sutorik, A. C.; Albritton-Thomas, J.; Kannewurf, C. R.; Kanatzidis, M. G. *J. Am. Chem. Soc.* **1994**, *116*, 7706–7713.

(29) Sörgel, T.; Nuss, J.; Wedig, U.; Kremer, R. K.; Jansen, M. *Mater. Res. Bull.* **2006**, *41*, 987–1000.

(30) Mansuetto, M. F.; Ibers, J. A. *J. Solid State Chem.* **1995**, *117*, 30–33.

(31) Selby, H. D.; Chan, B. C.; Hess, R. F.; Abney, K. D.; Dorhout, P. K. *Inorg. Chem.* **2005**, *44*, 6463–6469.

(32) Shannon, R. D. *Acta Crystallogr., Sect. A* **1976**, *32*, 751–767.

(33) Cody, J. A.; Ibers, J. A. *Inorg. Chem.* **1995**, *34*, 3165–3172.

(34) Sutorik, A. C.; Patschke, R.; Schindler, J.; Kannewurf, C. R.; Kanatzidis, M. G. *Chem.—Eur. J.* **2000**, *6*, 1601–1607.

(35) Narducci, A. A.; Ibers, J. A. *Inorg. Chem.* **2000**, *39*, 688–691.

(36) Sutorik, A. C.; Albritton-Thomas, J.; Hogan, T.; Kannewurf, C. R.; Kanatzidis, M. G. *Chem. Mater.* **1996**, *8*, 751–761.

(37) Huang, F. Q.; Mitchell, K.; Ibers, J. A. *Inorg. Chem.* **2001**, *40*, 5123–5126.

(38) Wells, D. M.; Jin, G. B.; Skanthakumar, S.; Haire, R. G.; Soderholm, L.; Ibers, J. A. *Inorg. Chem.* **2009**, *48*, 11513–11517.

(39) Kim, J.-Y.; Gray, D. L.; Ibers, J. A. *Acta Crystallogr., Sect. E* **2006**, *E62*, i124–i125.

(40) Zachariasen, W. H. *Acta Crystallogr.* **1948**, *1*, 265–268.

(41) Noël, H.; Padiou, J. *Acta Crystallogr., Sect. B* **1976**, *32*, 1593–1595.

(42) Jin, G. B.; Ringe, E.; Long, G. J.; Grandjean, F.; Sougrati, M. T.; Choi, E. S.; Wells, D. M.; Balasubramanian, M.; Ibers, J. A. *Inorg. Chem.* **2010**, *49*, 10455–10467.

(43) Oh, G. N.; Ibers, J. A. *Acta Crystallogr.* **2011**, *E67*, i9.

(44) Bugaris, D. E.; Wells, D. M.; Ibers, J. A. *J. Solid State Chem.* **2009**, *182*, 1017–1020.

(45) Gray, D. L.; Backus, L. A.; Krug von Nidda, H.-A.; Skanthakumar, S.; Loidl, A.; Soderholm, L.; Ibers, J. A. *Inorg. Chem.* **2007**, *46*, 6992–6996.

(46) O'Connor, C. J. *Prog. Inorg. Chem.* **1982**, *29*, 203–283.

(47) Kittel, C. *Introduction to Solid State Physics*, 7th ed.; Wiley: New York, 1996.

(48) Rüdorff, W.; Menzer, W. *Z. Anorg. Allg. Chem.* **1957**, *292*, 197–202.

(49) Levet, J.-C. *C. R. Seances Acad. Sci., Ser. C* **1969**, *268*, 703–705.

(50) Chen, C.-S.; Lee, S.-F.; Lii, K.-H. *J. Am. Chem. Soc.* **2005**, *127*, 12208–12209.

(51) Noël, H. *J. Less-Common Met.* **1980**, *72*, 45–49.

(52) Daoudi, A.; Noël, H. *J. Alloys Compd.* **1996**, *233*, 169–173.

(53) Center for X-ray Optics, X-ray Interactions with Matter, LBNL, Berkeley, CA, USA. http://www-cxro.lbl.gov/optical_constants (accessed June 2011).

(54) Wolska, A.; Bacewicz, R.; Filipowicz, J.; Attenkofer, K. *J. Phys.: Condens. Matter* **2001**, *13*, 4457–4470.

(55) Bugaris, D. E.; Copping, R.; Tyliszczak, T.; Shuh, D. K.; Ibers, J. A. *Inorg. Chem.* **2010**, *49*, 2568–2575.

(56) Grioni, M.; Goedkoop, J. B.; Schoorl, R.; de Groot, F. M. F.; Fuggle, J. C.; Schäfers, F.; Koch, E. E.; Rossi, G.; Esteva, J.-M.; Karnatak, R. C. *Phys. Rev. B* **1989**, *39*, 1541–1545.

(57) Pearce, C. I.; Pattrick, R. A. D.; Vaughan, D. J.; Henderson, C. M. B.; van der Laan, G. *Geochim. Cosmochim. Acta* **2006**, *70*, 4635–4642.

(58) De Nadaï, C.; Demourgues, A.; Grannec, J.; de Groot, F. M. F. *Phys. Rev. B* **2001**, *63*, 125123−1 - 125123−6.

(59) Folmer, J. C. W.; Jellinek, F. *J. Less-Common Met.* **1980**, *76*, 153–162.

(60) van der Laan, G.; Pattrick, R. A. D.; Charnock, J. M.; Grguric, B. A. *Phys. Rev. B* **2002**, *66*, 045104−1−045104−5.

(61) Pattrick, R. A. D.; van der Laan, G.; Vaughan, D. J.; Henderson, C. M. B. *Phys. Chem. Minerals* **1993**, *20*, 395–401.

(62) van der Laan, G.; Pattrick, R. A. D.; Henderson, C. M. B.; Vaughan, D. J. *J. Phys. Chem. Solids* **1992**, *53*, 1185–1190.

(63) Burns, W. L.; Ibers, J. A. *J. Solid State Chem.* **2009**, *182*, 1457–1461.

(64) Shuh, D. K.; Tyliszczak, T. Unpublished results.

(65) Copping, R.; Teat, S. J.; Janousch, M.; Tyliszczak, T.; Shuh, D. K. Manuscript in preparation.

(66) Eanes, M. E.; Schimek, G. L.; Kolis, J. W. *J. Chem. Crystallogr.* **2000**, *30*, 223–226.

(67) Teske, C. L.; Bensch, W. *Acta Crystallogr., Sect. E* **2006**, *62*, 26–28.

(68) Bondi, A. *J. Phys. Chem.* **1964**, *68*, 441–451.

(69) Jansen, M. *Angew. Chem., Int. Ed. Engl.* **1987**, *26*, 1098–1110.

(70) Burschka, C.; Bronger, W. *Z. Anorg. Allg. Chem.* **1977**, *430*, 61–65.

(71) Bronger, W.; Schils, H. *J. Less-Common Met.* **1982**, *83*, 287–291.

(72) Brown, I. D. *The Chemical Bond in Inorganic Chemistry, The Bond Valence Model*; Oxford University Press: New York, 2002.

(73) Hormillosa, C.; Healy, S.; Stephen, T. *Bond Valence Calculator*, V2.0, 1993.

(74) Eulenberger, G. *Acta Crystallogr., Sect. C* **1986**, *42*, 528–534.

(75) Beck, H. P.; Dausch, W. *Z. Naturforsch. B: Chem. Sci.* **1988**, *43*, 1547–1550.

(76) Moseley, P. T.; Brown, D.; Whittaker, B. *Acta Crystallogr.* **1972**, *B28*, 1816–1821.

(77) Zachariasen, W. H. *Acta Crystallogr.* **1949**, *2*, 291–296.

(78) Khodadad, P. *C. R. Hebd. Seances Acad. Sci.* **1959**, *249*, 694–696.

(79) Tougait, O.; Potel, M.; Levet, J. C.; Noël, H. *Eur. J. Solid State Inorg. Chem.* **1998**, *35*, 67–76.

(80) Julien, R.; Rodier, N.; Tien, V. *Acta Crystallogr., Sect. B* **1978**, *34*, 2612–2614.

(81) Rodier, N.; Tien, V. *Acta Crystallogr. Sect. B* **1976**, *32*, 2705–2707.

(82) Yao, J.; Jin, G. B.; Malliakas, C.; Wells, D. M.; Ellis, D. E.; Kanatzidis, M. G.; Ibers, J. A. Unpublished results.

(83) Savelsberg, G.; Schäfer, H. *Mater. Res. Bull.* **1981**, *16*, 1291–1297.

(84) Bronger, W.; Schils, H. *J. Less-Common Met.* **1982**, *83*, 279–285.

(85) Schils, H.; Bronger, W. *Z. Anorg. Allg. Chem.* **1979**, *456*, 187–193.

(86) Berger, R.; Meerschaut, A. *Eur. J. Solid State Inorg. Chem.* **1988**, *25*, 279–288.

(87) Spek, A. L. *PLATON*; Utrecht University: Utrecht, The Netherlands, 2008.

(88) Graves, C. R.; Scott, B. L.; Morris, D. E.; Kiplinger, J. L. *J. Am. Chem. Soc.* **2007**, *129*, 11914–11915.

(89) Graves, C. R.; Yang, P.; Kozimor, S. A.; Vaughn, A. E.; Clark, D. L.; Conradson, S. D.; Schelter, E. J.; Scott, B. L.; Thompson, J. D.; Hay, P. J.; Morris, D. E.; Kiplinger, J. L. *J. Am. Chem. Soc.* **2008**, *130*, 5272–5285.